

# Progressive regulation of Al sites and Cu distribution to increase hydrothermal stability of hierarchical SSZ-13 for the selective catalytic reduction reaction

Zhiqiang Chen, Tianle Ye, Hongxia Qu\*, Tenglong Zhu, Qin Zhong

School of Chemistry and Chemical Engineering, Nanjing University of Science and Technology, Nanjing 210094, China



## ARTICLE INFO

**Keywords:**  
NH<sub>3</sub>-SCR reaction  
SSZ-13  
Al sites  
Cu distribution  
Hydrothermal stability

## ABSTRACT

As a commercial catalyst for selective catalytic reduction of nitrogen oxides (NO<sub>x</sub>) with ammonia (NH<sub>3</sub>), hydrothermal stability is critical to the lifetime of copper-based SSZ-13. Adjusting the appropriate distribution of framework Al sites and the active copper ions can improve the hydrothermal stability of Cu-SSZ-13. Here we present a hierarchical SSZ-13 catalyst that prepared by the collaborative effect of two organic templates. The employ of C<sub>16</sub>H<sub>33</sub>-[N<sup>+</sup>-methylpiperidine] (C<sub>16</sub>MPBr) successfully introduced the hydrophobic mesoporous system into the catalyst. Detailed characterizations illustrate that the density of paired Al in the SSZ-13 framework increased with increasing content of C<sub>16</sub>MPBr in the crystalline gels. The increase in the content of paired Al conversely promotes the generation of more hydrothermally stable Cu<sup>2+</sup>-2Z species in the six-membered rings sites. This effectively suppresses the loss of active copper ions and dealumination of the framework during the hydrothermal aging, therefore, the hydrothermal stability of the catalyst is remarkably improved.

## 1. Introduction

Zeolites provide an efficient and convenient reaction platform for many catalytic reactions because of theirs ordered pore connectivity, excellent ion accommodation, plentiful acidity, and unique confinement effect [1–3]. They are diffusely applied in industrial applications such as gas adsorption and separation, organic shape-selective reactions, and environmental catalysis [4]. Moreover, after effective design and modification, zeolite can also exhibit unexpected performance in the fields of photocatalysis, electrocatalysis, and energy chemistry. For example, Tang et al. [5] synthesized periodic zeolite films by self-assembly of LTA zeolite hyperspheres; by adjusting the geometry of LTA zeolite spheres, a variety of light controllable manipulation was realized. Li and co-workers reported the synthesis of a variety of carbon-dots zeolites and used these zeolites to achieve room-temperature activated delayed fluorescence [6]. More recently, Yu et al. [7] used the zeolite membrane of lithium-ion exchange zeolite X as an inorganic solid electrolyte for the assembly of lithium-air batteries, which showed extremely low interface resistance and superior performance.

As an important branch of the zeolite family, small pore zeolites have become a research hotspot in recent years due to theirs advantages in

molecular shape-selective catalysis [8]. As one of the typical applications, copper-based SSZ-13 (Cu-SSZ-13) for NH<sub>3</sub>-SCR has recently obtained rapid development and achieved staged success by virtue of its commercialization in mobile source [9–11]. The atomic-level research progress on copper active sites in Cu-SSZ-13 provided great assistance and guidance for clarifying the reaction mechanism of NH<sub>3</sub>-SCR and indicating ways to improve its performance. For standard NH<sub>3</sub>-SCR reaction, the two types of copper active centers in Cu-SSZ-13 have been widely confirmed and universally recognized [12,13]. These two types of active centers are Cu<sup>2+</sup>-2Z located in the plane of the six-membered rings (6MR) and [Cu(OH)]<sup>+-Z</sup> located in the window of the eight-membered rings (8MR) of CHA cages, respectively [14]. Recent studies have shown that these two kinds of active centers have obvious differences in their resistance to hydrothermal aging and sulfur poisoning [15,16]. Compared to [Cu(OH)]<sup>+-Z</sup>, Cu<sup>2+</sup>-2Z is proven to have better hydrothermal stability. The relatively unstable [Cu(OH)]<sup>+-Z</sup> species will react with water vapor to form CuO<sub>x</sub> species in a high temperature and humid environment. The accumulation of CuO<sub>x</sub> clusters accelerates the dealumination of the zeolite framework because they can form inert CuAlO<sub>x</sub> species with extra-framework Al [17]. The resulting collapse of the zeolite framework, the loss of copper active centers and the loss of Brønsted acid sites lead to a decrease in the

\* Corresponding author.

E-mail address: [qxh@mail.njust.edu.cn](mailto:qxh@mail.njust.edu.cn) (H. Qu).

catalytic activity of Cu-SSZ-13 [18,19]. Thus, the resistance to hydrothermal aging is one of the key factors that affect the service life of Cu-SSZ-13. As a result, optimizing the distribution of copper active centers in Cu-SSZ-13 has become an important way to improve its performance.

Since the  $[\text{AlO}_4]^-$  in the zeolite framework provide the balance charges of the copper active centers, the distribution and location of the copper active centers in Cu-SSZ-13 are importantly related to the content and arrangement of Al in the zeolite framework. Earlier studies have proved that the capacity of copper active centers in Cu-SSZ-13 is positively correlated with the Al content of the zeolite framework, that is, the Si/Al ratio of the zeolite framework significantly affects the exchange volume and location distribution of copper active centers [20]. Gao et al. [21] reported the effect of changing the Si/Al ratio (Si/Al ratio from 6 to 35) of the zeolite framework on the position distribution of copper active centers in the condition of the same Cu/Al ratio. They found that the active copper species mainly occupy the cation sites of 6MR plane in the form of  $\text{Cu}^{2+}\text{-}2\text{Z}$  in samples with high content of framework Al (Si/Al = 6). However, in the samples with low content of framework Al (Si/Al = 35), limited by the scarcity of paired Al in the framework, the main active copper species is  $[\text{Cu}(\text{OH})]^{+}\text{-Z}$  occupying the 8MR window. Unfortunately, the scheme of adjusting the distribution of copper active centers by greatly regulating the framework Si/Al ratio to improve the performance of Cu-SSZ-13 does not seem feasible. This is mainly because the high Si/Al ratio (Si/Al > 25) limits the exchange of copper ions, thereby affecting the SCR activity of the catalyst; the lower Si/Al ratio (Si/Al < 8) may cause more easily dealuminated and degraded of the zeolite framework under severe conditions, thereby severely reducing the lifetime of the catalyst. However, the important value of this work is to establish an effective relationship between the Al content and arrangement of the framework and the distribution of copper active centers. This provides an enlightenment on whether it is possible to effectively change the Al arrangement in the framework without significantly changing the Si/Al ratio of the framework to achieve the purpose of affecting the distribution of copper active centers. Earlier studies by Gounder and co-workers found that in SSZ-13 crystallized with a fixed Si/Al ratio, the Al density of the framework increases linearly with the  $\text{Na}^+$  content in the crystallization medium [22]. Their recent studies have also discovered that the paired Al induced by  $\text{Na}^+$  is mainly distributed in the 6MR of the CHA framework [23]. On the contrary, the addition of  $\text{K}^+$  with a larger cation radius in the crystallization medium can induce more paired Al formed in the 8MR window of the CHA framework. Li et al. [24] studied the effects of different alkali metal ions ( $\text{Li}^+$ ,  $\text{Na}^+$ ,  $\text{K}^+$  and  $\text{Cs}^+$ ) on the Al distribution and copper ion positions in the framework of SSZ-13 and found that  $\text{Li}^+$  ions as a co-template significantly promoted the formation of paired Al in the framework, thereby induced a linear increase in the content of  $\text{Cu}^{2+}\text{-}2\text{Z}$  species at the 6MR sites. Different from the above studies of using inorganic cations as co-templates to regulate the Al arrangement of the framework and the distribution of copper species, Xiao et al. [25] reported two different crystallization pathways for the synthesis of SSZ-13 zeolite using organic templates. They confirmed that compared with SSZ-13 synthesized using conventional N, N, N-trimethyl-1-adamantanammonium hydroxide (TMAda-OH) as a template, SSZ-13 synthesized using N, N-dimethylcyclohexylammonium ( $\text{DMCHA}^+$ ) as an organic template would preferentially form 6MR units during the crystallization process. This caused the paired Al in this type of SSZ-13 mainly concentrate in 6MR plane, which in turn produces more  $\text{Cu}^{2+}\text{-}2\text{Z}$  species after copper exchange and improves the hydrothermal stability of the catalyst. These reports stimulate us realize that the progressive regulation of the framework Al distribution and copper active centers can be achieved through the important relationship between the framework Al arrangement and active copper sites, that is, by changing the synthesis environment of SSZ-13 to affect its framework Al arrangement, and then the distribution of copper active centers can be further regulated.

Here, a series of hierarchical SSZ-13 for  $\text{NH}_3\text{-SCR}$  were prepared by dual-template strategy using TMAda-OH and  $\text{C}_{16}\text{H}_{33}\text{-}[\text{N}^+\text{-methylpiperidine}]$  ( $\text{C}_{16}\text{MPBr}$ ) as templates. The framework Al arrangement of the obtained zeolites were explored in detail through cobalt ion titration, Fourier transform infrared spectra (FTIR) and diffuse reflectance ultraviolet-visible (DR UV-vis) spectra. The position and distribution of active copper ions in obtained zeolites and the influence of Al arrangement on the position selection of copper ions were further investigated. The effective relevance between the distribution of active copper ions and the arrangement of framework Al as well as the hydrothermal stability of the catalyst was established. The tandem relations of structure-active center-performance provides a new opportunity for the devise of new efficiency catalysts.

## 2. Experimental

### 2.1. Synthesis of $\text{C}_{16}\text{H}_{33}\text{-}[\text{N}^+\text{-methylpiperidine}]$

$\text{C}_{16}\text{H}_{33}\text{-}[\text{N}^+\text{-methylpiperidine}]$  (denoted as  $\text{C}_{16}\text{MPBr}$ ) were synthesized using a similar procedure described by Hensen et al. [26]. First, 100 ml of ethanol (99.9%, Aladdin) and 2.3 g of N-methylpiperidine (98%, Macklin) were added to a 500 ml triple flask and heated to 60 °C. Then, 6.1 g of 1-bromohexadecane (97%, Aladdin) was dropped into the mixture, further heating to 80 °C and stirring for 24 h. Next, the mixture was dried overnight in air at 60 °C. Finally, the solid product was washed 4 times with diethyl ether and dried for 12 h at 25 °C to obtain  $\text{C}_{16}\text{MPBr}$ .

### 2.2. Catalyst preparation

Hierarchical SSZ-13 was synthesized by a dual-template combining TMAda-OH as the SDA with  $\text{C}_{16}\text{MPBr}$  as the mesoporogen [27], details are shown in the [Supplementary Information](#).

The Co-form catalysts (denoted as Co-SSZ-13-20-0, Co-SSZ-13-17-3, and Co-SSZ-13-15-5, respectively) were prepared by ion-exchange method employing H-form catalysts (denoted as H-SSZ-13-20-0, H-SSZ-13-17-3, and H-SSZ-13-15-5, respectively) as the support. H-form catalysts were first ion-exchanged with  $\text{NaCl}$  (1 mol/L) solution at 80 °C for 8 h. Then, the catalysts were further ion-exchanged with aqueous  $\text{Co}(\text{NO}_3)_3$  solution (0.01 mol/L) at 80 °C for 12 h. This step was conducted three times to make the Co ion exchange complete [25]. Then the Co-form catalysts were washed, dried, and calcined at 550 °C for 6 h.

The H-form catalysts were ion-exchanged with  $\text{Cu}(\text{NO}_3)_2$  (0.1 mol/L) solution at 80 °C for 12 h to obtain Cu-form catalysts (denoted as Cu-SSZ-13-20-0, Cu-SSZ-13-17-3, and Cu-SSZ-13-15-5, respectively). Then the Cu-form catalysts were washed, dried, and calcined at 550 °C for 6 h.

For comparison, sample with TMAda-OH/ $\text{C}_{16}\text{MPBr}$  molar ratios = 10: 10 was prepared by the same method and denoted as SSZ-13-10-10.

### 2.3. Characterizations and catalyst activity evaluation

The detail of characterizations and catalyst activity evaluation are presented in the [Supplementary Material](#).

### 2.4. Density functional theory (DFT) calculations

Periodic supercell DFT calculations were performed with the Vienna Ab initio simulation package (VASP) under the Kohn-Sham formulation [28,29]. The lattice constants of CHA zeolite were fixed at values given in the International Zeolite Association database Formulation [30]. Atoms were permitted to fully relax during calculations. Other detailed information about calculations is shown in the [Supplementary Material](#).

### 3. Results and discussion

#### 3.1. Catalysts characterization

The structure and morphology of the hierarchical H-SSZ-13 catalysts were examined by X-ray powder diffraction (XRD) and Scanning electron microscopy (SEM). As shown in Fig. 1a, all catalysts showed a typical CHA framework structure and no other detectable impurities were formed [31]. This indicates that the adoption of C<sub>16</sub>MPBr hardly affects the conformation of CHA framework structure in this context and is a suitable mesoporous agent. Fig. 1b shows the low-angle XRD spectra of all catalysts. For H-SSZ-13 synthesized with pure TMAda-OH as template, the detected faint diffraction peak near 1.3° is attributed to the intergranular mesopores produced by accumulation of zeolite sheets. With the addition of C<sub>16</sub>MPBr as the mesoporogen, strong and broad diffraction peaks appeared in the spectra of H-SSZ-13-17-3 and H-SSZ-13-15-5, indicating the existence of mesopores guided by C<sub>16</sub>MPBr. In addition, the formation of the mesoporous system caused a slight decrease in the crystallinity of H-SSZ-13-17-3 and H-SSZ-13-15-5, which was confirmed by the faint decrease in the intensity of the observed XRD diffraction peaks in Fig. 1a.

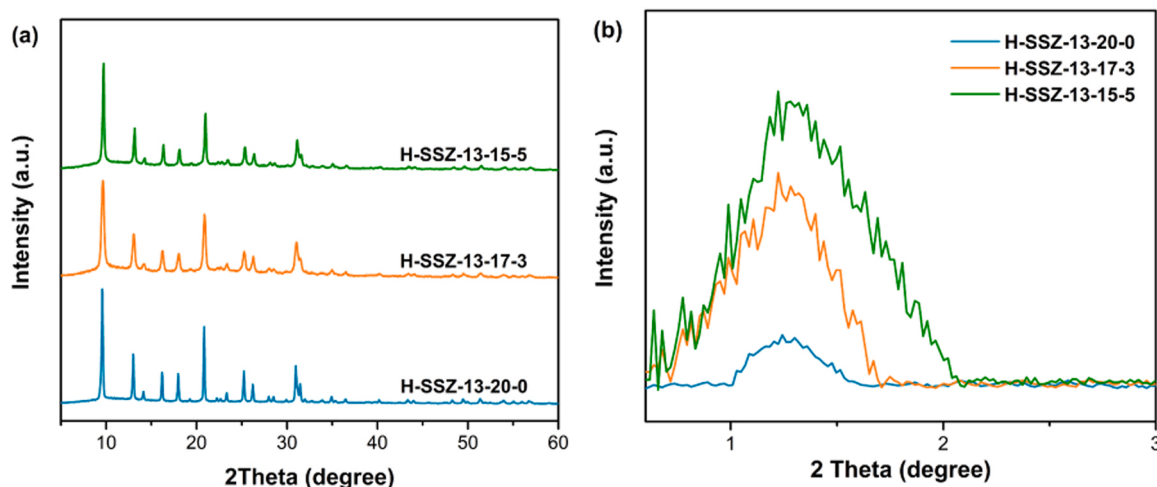
SEM microscopy images display that H-SSZ-13-20-0 synthesized with pure TMAda-OH as template exhibits a cubic shape ranging in size from 2 to 3 μm, which is stacked by nanoflakes (Fig. 2a,b). The cubic crystal surface is relatively smooth and the crystal size is uniform, with an average particle size of 2.6 μm. As the increase amount of C<sub>16</sub>MPBr mesoporogen in the crystalline gels, the morphology of the catalysts changes significantly. Zeolite particles are no longer stacked by flakes, but are stacked by small cubic crystals with a size of about 100 nm to form three-dimensional intergrowths, and obvious mesoporous pores appear between the primary cubic crystals. The size of the zeolite particles is also significantly smaller, which corresponds to the broadening of the diffraction peaks in the XRD spectra. This obvious difference in morphology should be due to the change of the species interaction force in the crystalline gels by the C<sub>16</sub>MPBr template, thus affecting the growth rate of crystals in different directions.

Fig. S1 and Fig. 3 shows the N<sub>2</sub> adsorption isotherms, pore size distribution and pore volume of all catalysts. As shown in Fig. S1, H-SSZ-13-20-0 exhibits a type I isotherm characteristic of a microporous material [32]. The weak H4 hysteresis loop appearing at higher relative pressure ( $P/P_0 > 0.5$ ) is due to a small amount of intergranular mesopores produced by the stacking of flakes, and the mesopore diameter is about 3.9 nm. The type IV isotherms display by H-SSZ-13-17-3 and H-SSZ-13-15-5 indicate their mesoporous properties. The pore size distribution curves of all catalysts are shown in Fig. 3a. A characteristic

pore diameter of 0.38 nm attributed to SSZ-13 was observed in the pore size distribution curves of all catalysts [33]. For H-SSZ-13-17-3, the new pore size at 3.6 nm is ascribed to the intergranular mesopores guided by C<sub>16</sub>MPBr. With the increase amount of C<sub>16</sub>MPBr mesoporogen in the crystalline gels, widely distributed mesopores centered at 10 nm were observed, indicating the stronger mesopore characteristics of H-SSZ-13-15-5. This can be further confirmed by the pore volume curves (Fig. 3b), as H-SSZ-13-15-5 displays a higher mesopore volume. The order of the mesoporous pore volume is as follows: H-SSZ-13-15-5 > H-SSZ-13-17-3 > H-SSZ-13-20-0. These discussions fit the results of XRD and SEM, supporting the conclusion of intergranular mesoporous system directed by the C<sub>16</sub>MPBr mesoporogen.

To observe the coordination of Al in the hierarchical H-SSZ-13 catalysts, the <sup>27</sup>Al Solid-state magic-angle spinning nuclear magnetic resonance (<sup>27</sup>Al MAS NMR) was measured, and the spectra are displayed in Fig. 4a. The features near 58 and 0 ppm are ascribed to the four-coordinated framework Al, and six-coordinated extra-framework Al, respectively [15,34]. It should be noted that the intensity of signal center at 0 ppm is very weak (< 2%), indicating Al element have been almost amalgamated into the CHA framework in the form of tetrahedral structured. This demonstrates that the formation of mesoporous system did not result the loss of framework Al in the hierarchical H-SSZ-13 catalysts.

To assess the coordination of Si species in the hierarchical H-SSZ-13 catalysts, the <sup>29</sup>Si MAS NMR measurements were further carried out with the spectra are shown in Fig. 4b. Three <sup>29</sup>Si MAS NMR features at – 101.5, – 105.5, and – 111.0 ppm are detected. Previous studies have shown that the <sup>29</sup>Si MAS NMR resonance between – 92 and – 100 ppm reflects the coordination of Si (2Si, 2Al), and the <sup>29</sup>Si MAS NMR feature between – 100 and – 107 ppm is ascribed to Si (3Si, 1Al) or Si (3Si, OH), while the <sup>29</sup>Si MAS NMR feature below – 110 ppm is attributed to Si (4Si, 0Al) coordination [35,36]. Thus, in the present spectra, the <sup>29</sup>Si MAS NMR feature center at – 111.0 ppm can be assigned to tetrahedral Si in the form of Si (4Si, 0Al). To identify the feature of Si (3Si, OH), the <sup>29</sup>Si cross-polarization/MAS NMR experiment were performed on H-SSZ-13-20-0 with the result is shown in Fig. S2. The obvious increase of the feature near – 101.5 ppm in the cross-polarization spectrum indicates that the measured <sup>29</sup>Si MAS NMR signal at – 101.5 ppm should be assigned to Si (3Si, OH). Therefore, two <sup>29</sup>Si MAS NMR resonance features appearing at – 101.5 and – 105.5 ppm should be attributed to Si (3Si, OH) and Si (3Si, 1Al), respectively. The Si/Al ratio obtained from the ICP-AES take a good agreement with the Si/Al<sub>F</sub> ratio calculated from the <sup>29</sup>Si MAS NMR spectra, which confirms the allocation of <sup>29</sup>Si MAS NMR resonance features (Table 1).



**Fig. 1.** (a) XRD patterns of H-SSZ-13-20-0, H-SSZ-13-17-3, and H-SSZ-13-15-5; (b) Low-angle XRD patterns of H-SSZ-13-20-0, H-SSZ-13-17-3, and H-SSZ-13-15-5.

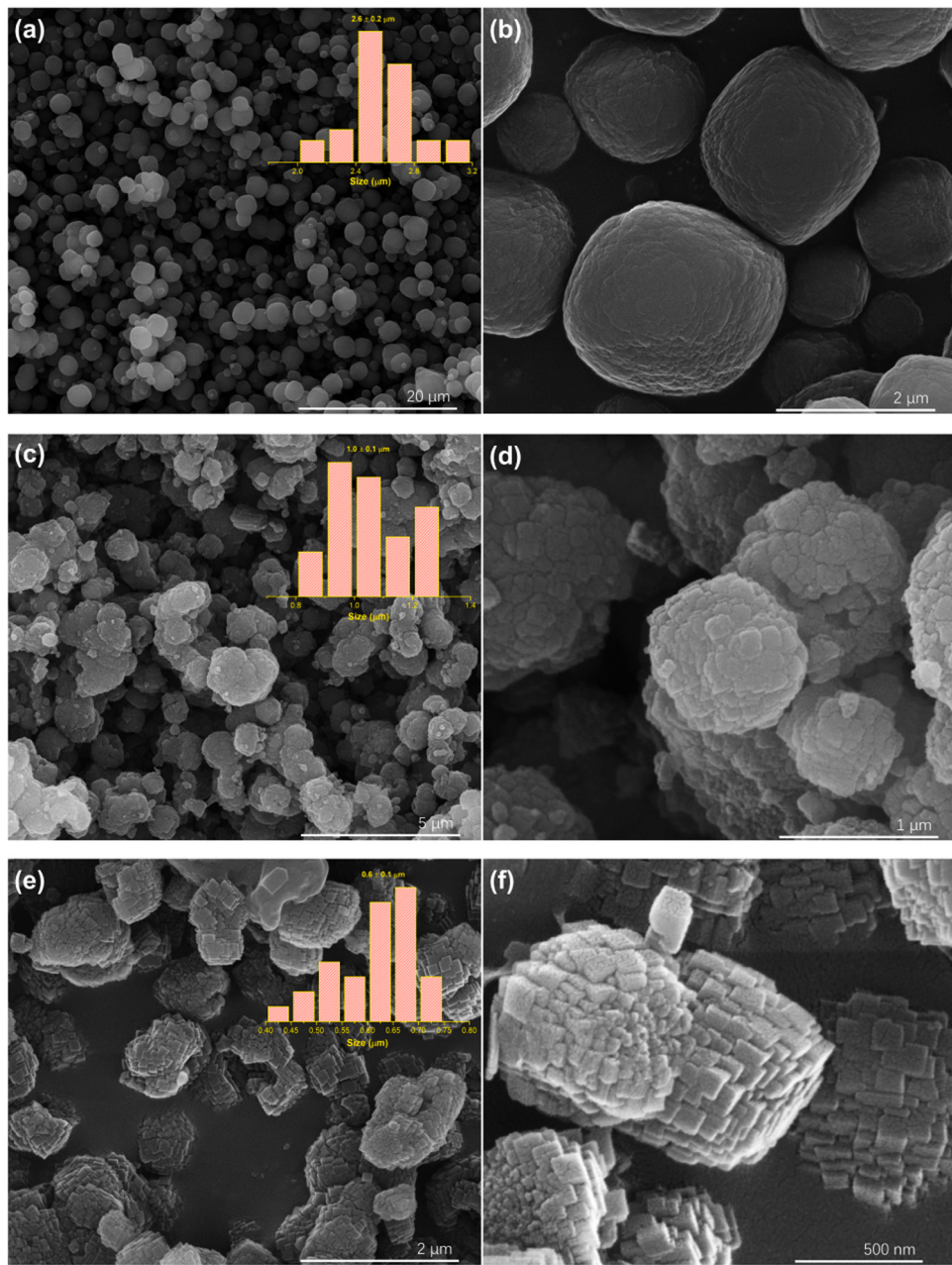


**Fig. 2.** SEM images of (a, b) H-SSZ-13-20-0, (c, d) H-SSZ-13-17-3 and (e, f) H-SSZ-13-15-5.

### 3.2. The effect of $C_{16}MPbr$ co-template on the Al distribution of the hierarchical catalysts

The distribution of Al sites in zeolite and the cooperation or isolation between them show an important influence on its catalytic properties. According to the proximity of the acid center and the accommodation of  $Me^{2+}$  (e.g.,  $Cu^{2+}$ ,  $Co^{2+}$ ,  $Zn^{2+}$ ) in the cation sites, the Al sites in the zeolite framework can be reasonably divided into paired Al ( $Al_{Pair}$ ), close unpaired Al ( $Al_{Close}$ ) and isolated Al ( $Al_{Isolated}$ ), respectively. Since all T sites of CHA configuration zeolite are crystallographic ally equivalent [37], the Al distribution of this type of zeolite is simpler than that of other types of zeolites. Excluding the Al arrangement ( $Al-O-Al$ ) that cannot exist in zeolite according to Löwenstein's rule [38], there should usually be three types of silicon-aluminum arrangement sequence in SSZ-13,  $Al-O-Si-O-Al$ ,  $Al-O-(Si-O)_2-Al$  and  $Al-O-(Si-O)_3-Al$ , respectively. Previous reports indicate that the  $Al-O-Si-O-Al$  sequence in SSZ-13 can be monitored by the signal of Si (2Si, 2Al) in  $^{29}Si$  NMR [35,39]. This Al

sequence usually only appears in aluminum-rich SSZ-13 ( $Si/Al < 8$ ) [40], and there is no Si (2Si, 2Al) signal in all samples reported in present research (Fig. 4b). Therefore, in the current study, the  $Al-O-Si-O-Al$  arrangement that may appear in the samples can be reasonably excluded, and the  $Al-O-(Si-O)_n-Al$  ( $n \geq 2$ ) arrangement will be further discussed.

For the various Al sites in the  $Al-O-(Si-O)_n-Al$  ( $n \geq 2$ ) arrangement, previous study by Sklenak and co-workers suggested that they can be distinguished by whether they can accommodate bare  $Co^{2+}$  ions [35, 41]. Paired Al corresponds to two aluminum atoms separated by silicon atoms that can produce cation sites capable of contain bare  $Co^{2+}$  ions in dehydrated zeolites. Al atoms that cannot accommodate bare  $Co^{2+}$  ions due to long distance or facing different channels are defined as non-Al pairs ( $Al_{Isolated}$  or  $Al_{Close}$ ). In this case, Paired Al can be divided into three types:  $\sigma$ ,  $\tau$  ( $\tau^{2Si}$  and  $\tau^{3Si}$ ) and  $\omega$ -types, respectively, according to different relative positions, as shown in Fig. S3. Among them, type- $\sigma$  is that two Al atoms seated in the same 6MR plane, type- $\tau$  is that two Al

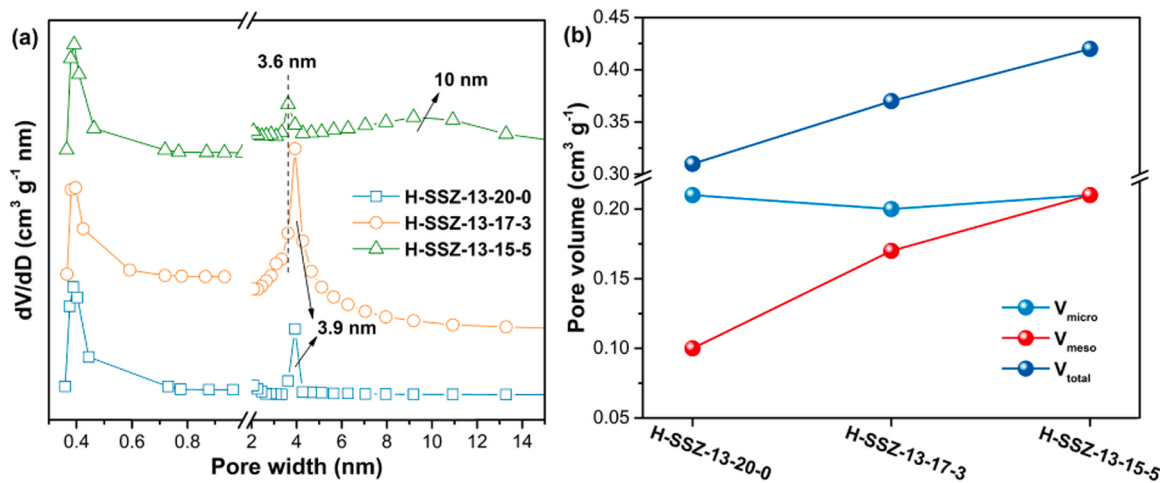


Fig. 3. (a) Pore size distribution of H-SSZ-13-20-0, H-SSZ-13-17-3, and H-SSZ-13-15-5; (b) pore volume of H-SSZ-13-20-0, H-SSZ-13-17-3, and H-SSZ-13-15-5.

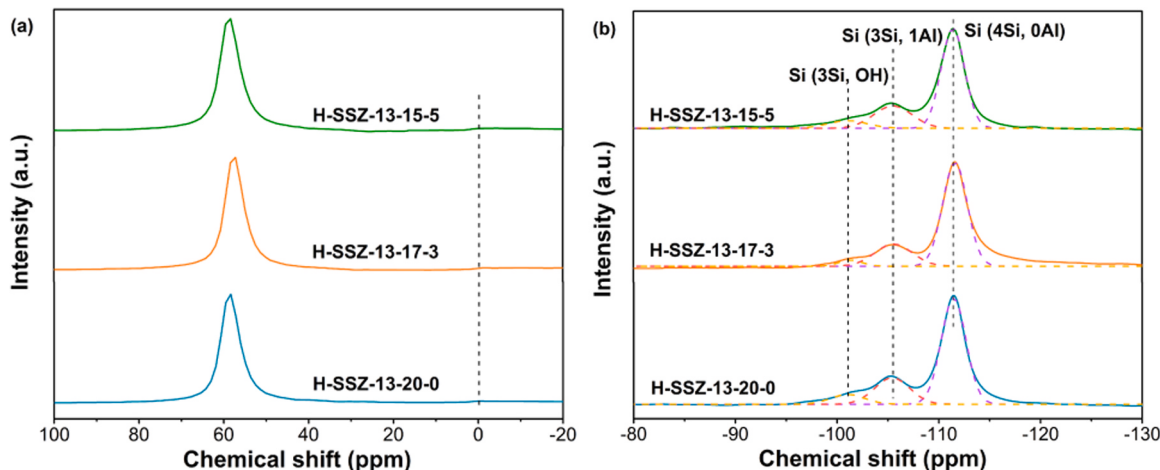


Fig. 4. (a)  $^{27}\text{Al}$  and (b)  $^{29}\text{Si}$  MAS NMR of H-SSZ-13-20-0, H-SSZ-13-17-3, and H-SSZ-13-15-5.

Table 1

Chemical compositions of different samples.

Samples	Si/Al <sup>a</sup>	Si/Al <sub>F</sub> <sup>b</sup>	Cu content (wt%) <sup>a</sup>	Cu/Al
SSZ-13-20-0	19.3	19.9	1.48	0.21
SSZ-13-17-3	19.1	20.3	1.51	0.21
SSZ-13-15-5	19.0	19.7	1.56	0.21

<sup>a</sup> Determined by ICP-AES.

<sup>b</sup> Determined by  $^{29}\text{Si}$  MAS NMR spectroscopy.

atoms seated in the same 8MR plane, and type- $\omega$  is that two Al atoms are located on different rings of a double six-membered prism [35,39]. Though the previous results show that the introduction of C<sub>16</sub>MPBr in the crystalline gels does not change the elemental composition of the catalyst (the similar Si/Al ratio) while guiding the formation of mesoporous system, its influence on the Al distribution of hierarchical SSZ-13 catalysts should be further studied.

Cobalt-ion exchange and quantitative titration of cobalt ions are effective and accurate methods to determine the type and distribution of Al sites in the zeolite framework [42]. All samples were subjected to three repeated cobalt-ion exchanges to ensure that the cobalt ions reached the maximum exchange capacity. Table 2 shows the Al content and the corresponding Co/Al ratio of all samples measured by ICP-AES. The trend of Co/Al ratio is as follows: Co-SSZ-13-15-5 (0.29) > Co-SSZ-13-17-3 (0.19) > Co-SSZ-13-20-0 (0.05). Therefore, the

Table 2

The distribution of framework Al in hierarchical SSZ-13 catalysts.

Samples	Al mmol/g <sup>a</sup>	Co/Al <sup>a</sup>	Co <sub>T-O-T</sub> mmol/g <sup>b</sup>	Al <sub>Isolated</sub> (%)	Al <sub>Close</sub> (%)	Al <sub>Pair</sub> (%)
Co-SSZ-13-20-0	1.09	0.05	0.032	90	4	6
Co-SSZ-13-17-3	1.11	0.19	0.153	62	10	28
Co-SSZ-13-15-5	1.18	0.29	0.237	42	18	40

<sup>a</sup> Determined by ICP-AES.

<sup>b</sup> Determined by the T-O-T vibrations of FTIR spectra of cobalt-exchanged zeolites.

proportion of Al<sub>Isolated</sub> in the samples can be determined according to Eq. (1):

$$[\text{Al}_{\text{Isolated}}] = [\text{Al}_F] - 2[\text{Co}_{\text{Max}}] \quad (1)$$

where [Al<sub>F</sub>] is the content of framework Al, and [Co<sub>Max</sub>] is the content of Co in the zeolites after fully exchanged.

The results show that the content of Al<sub>Isolated</sub> in Co-SSZ-13-20-0 is the highest, followed by Co-SSZ-13-17-3, and the content of Al<sub>Isolated</sub> in Co-SSZ-13-15-5 is the least (Table 2). This shows that the introduction of C<sub>16</sub>MPBr in the crystalline gels can effectively adjust the distribution of

Al in the catalyst. The use of more C<sub>16</sub>MPBr can cause a more concentrated distribution of Al in the catalysts.

The framework T-O-T vibration of dehydrated cobalt-exchanged zeolites can effectively estimate the proportion of paired Al in the zeolites. Since the dehydrated cobalt zeolites include only bare cobalt ions that can balance the negative charges generated by the paired Al, and the extinction coefficient of the T-O-T vibrations for cobalt ions in each position is very similar in SSZ-13, the total intensity of the T-O-T vibration signals of all cobalt ions can be used for measuring the total concentration of bare Co<sup>2+</sup> cations, and then obtained the total concentration of paired Al [35,39]. In this way, three different types of Al sites (Al<sub>Pair</sub>, Al<sub>Close</sub>, and Al<sub>Isolated</sub>) in the SSZ-13 can be effectively identified and quantified. Fig. 5a shows the FTIR spectra of all dehydrated cobalt-exchanged zeolites. The T-O-T framework vibration signals between 970 cm<sup>-1</sup> and 870 cm<sup>-1</sup> proved the presence of bare cobalt cations. There are obvious differences in the intensity of the T-O-T vibration signals of the cobalt ions in the three catalysts. The signal intensity of the T-O-T vibration follow the order: Co-SSZ-13-15-5 > Co-SSZ-13-17-3 > Co-SSZ-13-20-0. Using the extinction coefficient (30 cm μmol<sup>-1</sup>) of the T-O-T vibration signal reported by Sklenak and co-workers together with the total area of the T-O-T vibration signals, the [Co<sub>T-O-T</sub>] concentration of all samples can be roughly calculated (Table 2) [35]. Thus, the concentration of Al<sub>Pair</sub> can be given by Eq. (2) and the concentration of Al<sub>Close</sub> can be supplied by Eq. (3):

$$[\text{Al}_{\text{Pair}}] = 2[\text{Co}_{\text{T-O-T}}] \quad (2)$$

$$[\text{Al}_{\text{Close}}] = 2[\text{Co}_{\text{Max}}] - 2[\text{Co}_{\text{T-O-T}}] \quad (3)$$

where [Co<sub>T-O-T</sub>] is the bare Co<sup>2+</sup> cations concentration provided by total intensity of T-O-T vibration.

Table 2 shows the percentage of Al<sub>Pair</sub> and Al<sub>Close</sub> in all samples. As expected, the percentage of Al<sub>Pair</sub> in Co-SSZ-13-15-5 is the highest (40%), while only 6% Al<sub>Pair</sub> in the Co-SSZ-13-20-0 without using C<sub>16</sub>MPBr as co-template. This further confirms the regulation of C<sub>16</sub>MPBr co-template on the distribution of Al sites in the SSZ-13, that is, within a certain range, the content of Al<sub>Pair</sub> in the synthesized SSZ-13 increased with the increase in the amount of C<sub>16</sub>MPBr used. This significant increase in the content of paired Al can promote catalytic reactions that require multiple acidic sites to cooperate, and improve the ability of the zeolites to accommodate Me<sup>2+</sup> metal ions, which is critical for some catalytic processes (e.g., selective catalytic reduction, selective catalytic oxidation, NO<sub>x</sub> storage reduction).

In addition to the quantification of paired Al, the framework T-O-T vibration of dehydrated cobalt zeolites can also distinguish various types

of paired Al ( $\sigma$ ,  $\tau$  ( $\tau^{2\text{Si}}$  and  $\tau^{3\text{Si}}$ ) and  $\omega$ ) according to the positions of the vibration signal. Fig. S4 shows the peak fitting results of the T-O-T vibration spectra of the three catalysts. The peaks centered at 895 cm<sup>-1</sup>, 907 cm<sup>-1</sup>, 924 cm<sup>-1</sup> and 948 cm<sup>-1</sup> represents the  $\sigma$ -type Al<sub>Pair</sub>,  $\omega$ -type Al<sub>Pair</sub>,  $\tau^{2\text{Si}}$ -type Al<sub>Pair</sub> and  $\tau^{3\text{Si}}$ -type Al<sub>Pair</sub>, respectively [35]. Fig. 5b displays the peak area of different types Al<sub>Pair</sub> by deconvoluting the fitted spectra. It should be noted that no signal of  $\tau$ -types ( $\tau^{2\text{Si}}$  and  $\tau^{3\text{Si}}$ ) Al<sub>Pair</sub> were detected in Co-SSZ-13-20-0, which is due to the low content of Al<sub>Pair</sub> in Co-SSZ-13-20-0. This also shows that there are differences in the formation of these four different types of Al<sub>Pair</sub>. The  $\sigma$ -type Al<sub>Pair</sub> seated in the same 6MR plane and the  $\omega$ -type Al<sub>Pair</sub> seated in the D6R double prism can be formed preferentially.

The DR UV-Vis spectroscopy of dehydrated cobalt-exchanged zeolites further studied the distribution of paired Al in the catalysts (Fig. 6a). No obvious absorption bands appear between 25,000 and 30,000 cm<sup>-1</sup>, indicates that there are almost no cobalt oxides in all cobalt-exchanged zeolites [24]. The specificity of d-d transition absorption bands for cobalt ions between 14,500 and 25,000 cm<sup>-1</sup> can clearly reflect the cobalt ions at different cation sites, and then distinguish different types of paired Al [25]. Table S1 shows the different Al sites represented by each absorption band. It is worth noting that Co-SSZ-13-15-5 still displays the highest intensity of absorption band, followed by Co-SSZ-13-17-3 and Co-SSZ-13-20-0, respectively. This is consistent with the results of FTIR spectra, further confirming the significant difference in the proportion of paired Al in the three catalysts. Gaussian decomposition fitting was performed on the d-d absorption bands of all samples to meet the description of different paired Al distributions, and the results are shown in Fig. S5. Simultaneously, Gaussian integration is performed for each decomposed spectral line and the proportion of all paired Al distributions is counted (Fig. 6b). In line with the results of FTIR, no  $\tau$ -type Al<sub>Pair</sub> absorption bands appear in the spectrum of Co-SSZ-13-20-0 sample and the absorption bands proportion of the  $\tau$ -types Al<sub>Pair</sub> in Co-SSZ-13-17-3 is lower than that of Co-SSZ-13-15-5, especially the  $\tau^{3\text{Si}}$ -type Al<sub>Pair</sub>. This further illustrates the formation advantage of paired Al species on 6MR. This advantage causes the preferential formation of  $\sigma$ -type and  $\omega$ -type Al<sub>Pair</sub> species in the SSZ-13 when the Al distribution is relatively concentrated, and the content of these two types of species will also be higher.

Fig. 7 summarized the relative formation energies of different types Al<sub>Pair</sub> in SSZ-13 calculated by density functional theory (DFT) method. Compared with  $\tau$ -types Al<sub>Pair</sub>, the formation energy of  $\sigma$ -type and  $\omega$ -type Al<sub>Pair</sub> species is lower. The results show that paired Al arrangement are easier to form on 6MR plane or D6R prism, which explains the results detected in FTIR and DR UV-Vis spectra.

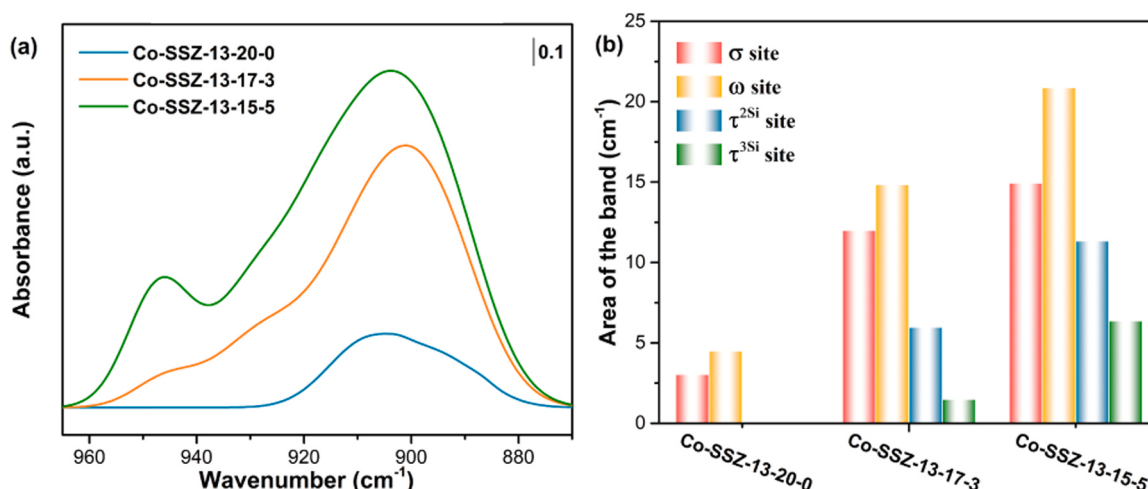


Fig. 5. (a) T-O-T vibration regions of the FTIR spectra and (b) peak area of different types paired Al of Co-SSZ-13-20-0, Co-SSZ-13-17-3, and Co-SSZ-13-15-5.

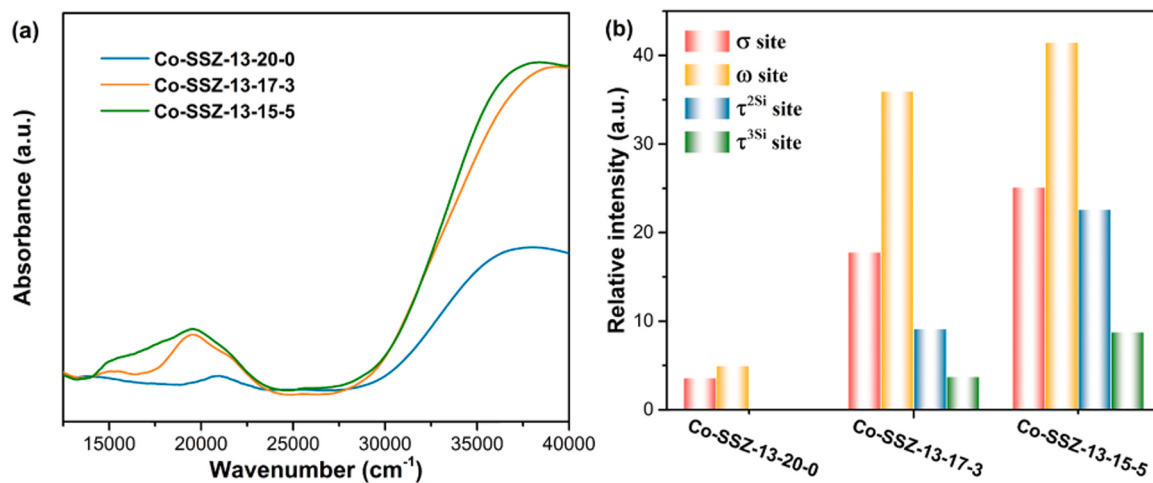


Fig. 6. (a) DR UV-Vis spectra and (b) relative intensity of different types paired Al of Co-SSZ-13-20-0, Co-SSZ-13-17-3, and Co-SSZ-13-15-5.

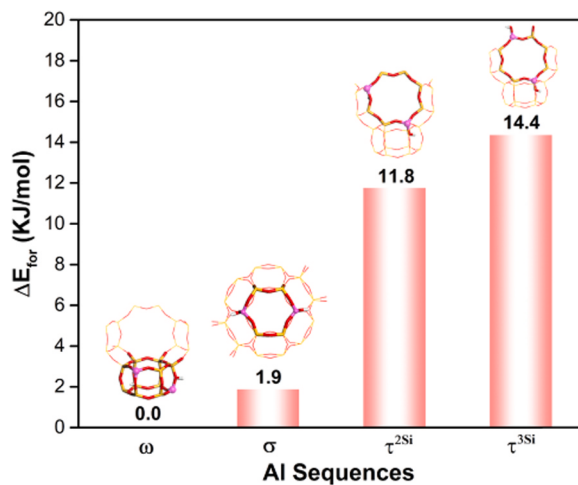


Fig. 7. Relative formation energies of different types paired Al in SSZ-13 zeolite, aluminum atoms are in pink. (For interpretation of the references to color in this figure legend, the reader is referred to the web version of this article.)

### 3.3. Dominant 6MR distribution of copper ions determined by Al distribution

To clarify the effect of Al arrangement on the distribution of active copper ions, a set of hierarchical Cu-SSZ-13 with similar copper loadings were prepared by ion-exchange method. Hydrogen temperature-programmed reduction ( $\text{H}_2\text{-TPR}$ ), In situ diffuse reflectance infrared Fourier transform spectroscopy of  $\text{NH}_3$  ( $\text{NH}_3\text{-DRIFTS}$ ) and Electron paramagnetic resonance (EPR) characterization techniques were used to probe the location and distribution of active copper ions of hierarchical Cu-SSZ-13.

We first used the DFT method to calculate the relative binding energy of  $\text{Cu}^{2+}\text{-2Z}$  species under various possible Al arrangements, the results are shown in Fig. 8. Note that the  $\omega^{3\text{Si}}$ -type Al arrangement is not defined as paired Al, since the two Al atoms are separated, but the two Al atoms in this arrangement possess the ability to accommodate  $\text{Cu}^{2+}\text{-2Z}$  ions. The order of the bonding tightness of  $\text{Cu}^{2+}\text{-2Z}$  under various Al arrangements is as follows:  $\sigma > \omega > \omega^{3\text{Si}} > \tau^{2\text{Si}} > \tau^{3\text{Si}}$ . This indicates that  $\text{Cu}^{2+}\text{-2Z}$  ions are more likely to seat at the cation sites of 6MR, that is, compared to the 8MR sites ( $\tau^{2\text{Si}}$  and  $\tau^{3\text{Si}}$ ), the Al sites of 6MR ( $\sigma$ ,  $\omega$  and  $\omega^{3\text{Si}}$ ) provide thermodynamically more stable cation sites [43].

$\text{H}_2\text{-TPR}$  can effectively study the location and properties of various

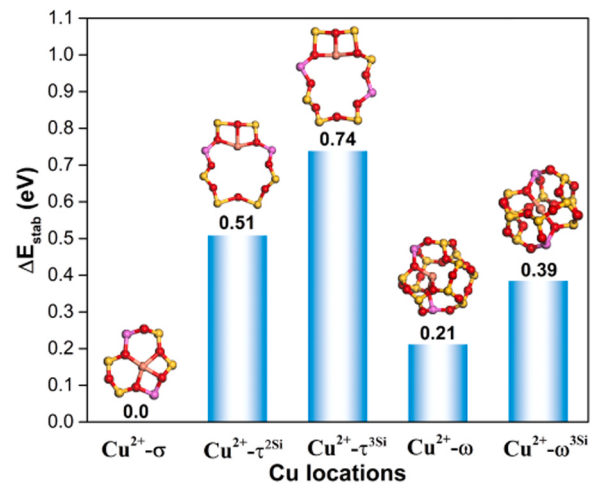


Fig. 8. Relative binding energy of  $\text{Cu}^{2+}\text{-2Z}$  under different possible Al arrangements in SSZ-13 zeolite.

copper species in zeolites. Fig. 9 shows the  $\text{H}_2\text{-TPR}$  profiles of the hierarchical Cu-SSZ-13. For all samples, the  $\text{H}_2$  consumption peak appearing at around  $250^\circ\text{C}$  (peak a) is related to the reduction of isolated copper ions in the form of  $[\text{Cu}(\text{OH})]^{+}\text{-Z}$  seat at the cation sites of the 8MR window [44]. The  $\text{H}_2$  consumption peak of  $\text{Cu}^{2+}\text{-2Z}$  ions seated at the cation sites of 6MR appears near  $360^\circ\text{C}$  (peak b) [10]. No signal related to the reduction of  $\text{CuO}_x$  species (around  $300^\circ\text{C}$ ) is detected [45], indicating that the copper species in all samples were almost located at the cation sites. It is worth noting that the peak intensities of the two active copper species on different samples are significantly different. To better discuss the distribution of active copper species, the deconvolution of the  $\text{H}_2\text{-TPR}$  profiles were taken, and the results are shown in Fig. 9b. For Cu-SSZ-13-20-0, the relative proportion of  $[\text{Cu}(\text{OH})]^{+}\text{-Z}$  species is 81%, which indicates that most of the copper ions in Cu-SSZ-13-20-0 are located in the cation sites of 8MR window, and the balance charge was provided by isolated Al atom. This is due to the low content of paired Al in Cu-SSZ-13-20-0. Though  $\text{Cu}^{2+}\text{-2Z}$  can be preferentially combined from a thermodynamic point of view, owing to the lack of paired Al arrangements that balance its double positive charges in the framework, it is difficult for active copper species to occupy the cation sites of 6MR in the form of  $\text{Cu}^{2+}\text{-2Z}$ . On the contrary, because of the high content of paired Al in 6MR, more copper species in Cu-SSZ-13-15-5 can occupy the 6MR sites in the form of  $\text{Cu}^{2+}\text{-2Z}$  (74%). This shows that different Al distribution can indeed effectively affect the

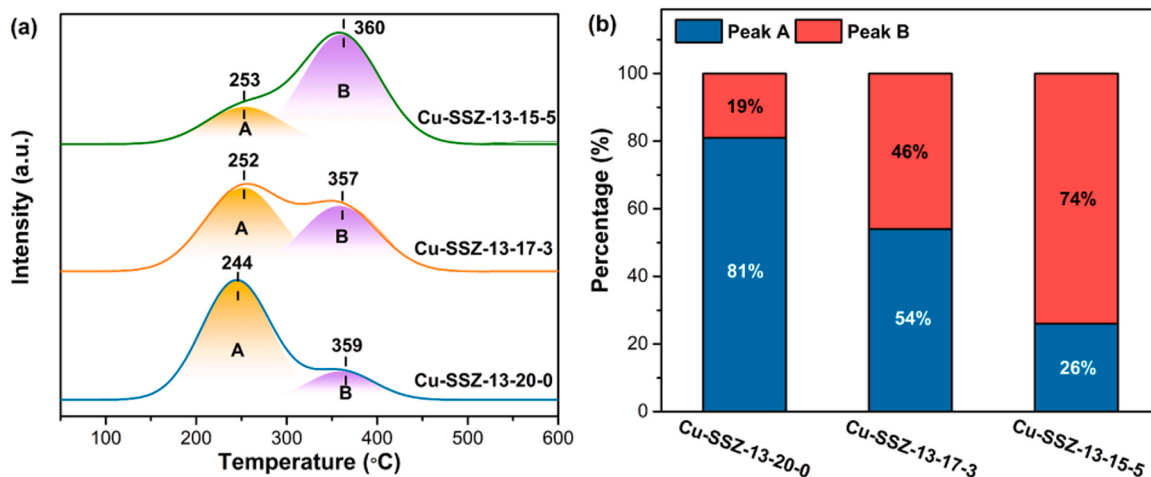


Fig. 9. (a) H<sub>2</sub>-TPR profiles and (b) the percentage of different types Cu ions of Cu-SSZ-13-20-0, Cu-SSZ-13-17-3, and Cu-SSZ-13-15-5.

distribution of active copper centers. This also indicates that the introduction of the C<sub>16</sub>MPBr co-template in the crystalline gels not only adjusts the Al distribution of the zeolite framework to induce the generation of more paired Al, but also further determines the effective regulation of the distribution of Cu ions. The T-O-T vibrations of Cu ions shown in the NH<sub>3</sub>-DRIFTS spectra also confirmed the above conclusions. As shown in Fig. 10a, two absorption bands are resolved at approximately 907 and 958 cm<sup>-1</sup>, which are attributed to the tetrahedral T-O-T framework vibration perturbed by the Cu<sup>2+</sup>-2Z and [Cu(OH)]<sup>+-Z</sup> species, respectively [24,46]. The Gaussian deconvolution of these two absorption bands shows that the proportion of Cu<sup>2+</sup>-2Z species increases with the increase in the amount of C<sub>16</sub>MPBr co-template used (Fig. 10b).

The position and coordination of copper species in the hierarchical Cu-SSZ-13 are further clarified by EPR. Note that CuO<sub>x</sub> and Cu<sup>+</sup> species are EPR-silent due to the antiferromagnetic effect. After dehydration, [Cu(OH)]<sup>+-Z</sup> species converts from [Cu(OH)(H<sub>2</sub>O)<sub>5</sub>]<sup>+</sup> will also lose EPR response owing to the pseudo Jahn-Teller effect [15,33,47]. Therefore, Cu<sup>2+</sup>-2Z and [Cu(OH)]<sup>+-Z</sup> can be distinguished by the EPR response of hydrated and dehydrated Cu-SSZ-13. Fig. 11a shows the EPR spectra of hydrated and dehydrated samples recorded at 140 K. The EPR signal intensities of all hydrated samples are very close, indicating that the content of Cu species in all hydrated catalysts is similar, which is consistent with the measurement results of ICP-AES. By quadratic integration of the EPR spectra of hierarchical Cu-SSZ-13 catalysts, the relative intensities of the two types ([Cu(OH)]<sup>+-Z</sup> and Cu<sup>2+</sup>-2Z) of active

copper species were obtained with the results are displayed in Fig. 11b. In line with the results shown by H<sub>2</sub>-TPR and NH<sub>3</sub>-DRIFTS, due to the significant increase in the content of paired Al in the framework, the relative intensity of Cu<sup>2+</sup>-2Z in Cu-SSZ-13-15-5 is the highest, followed by Cu-SSZ-13-17-3, while Cu-SSZ-13-20-0 only contains a small amount of Cu<sup>2+</sup>-2Z species. This shows the strong correlation between the Cu<sup>2+</sup>-2Z ions and the paired Al arrangement in the zeolite framework. This further confirmed the variety of Al distribution in zeolite framework caused by C<sub>16</sub>MPBr and the dominant distribution of Cu<sup>2+</sup>-2Z seated at ion sites of 6MR caused by the change in the content of paired Al. That is to say, the C<sub>16</sub>MPBr added to the crystalline gel promotes the generation of more paired Al species in the zeolite framework, especially the paired Al species in the 6MR plane, by guiding the formation of the mesoporous system. The increase in the concentration of paired Al causes more isolated copper ions to occupy the cationic sites of 6MR plane, resulting in a distribution of copper species dominated by Cu<sup>2+</sup>-2Z species in Cu-SSZ-13-15-5.

#### 3.4. Ammonia selective catalytic reduction performance and superiority hydrothermal stability of the hierarchical catalysts

The NO<sub>x</sub> conversion of the hierarchical Cu-SSZ-13 catalysts before and after hydrothermal aging is shown in Fig. 12a. Though the fresh catalysts maintained good activity, the SCR activity of different samples show obvious differences after hydrothermal aging (10% H<sub>2</sub>O/N<sub>2</sub>) at

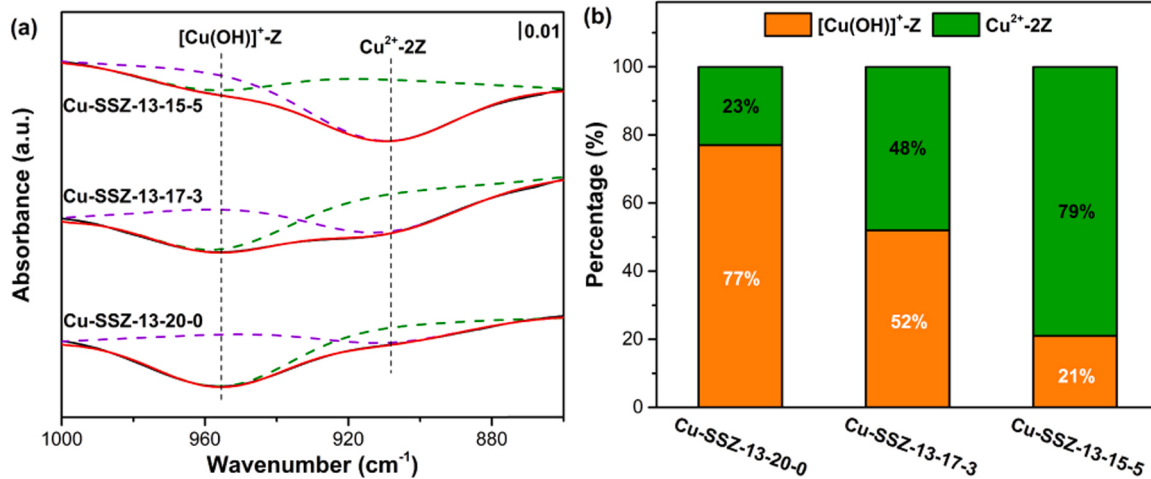


Fig. 10. (a) T-O-T vibration regions of the NH<sub>3</sub>-DRIFTS spectra and (b) the fitting results of Cu-SSZ-13-20-0, Cu-SSZ-13-17-3, and Cu-SSZ-13-15-5.

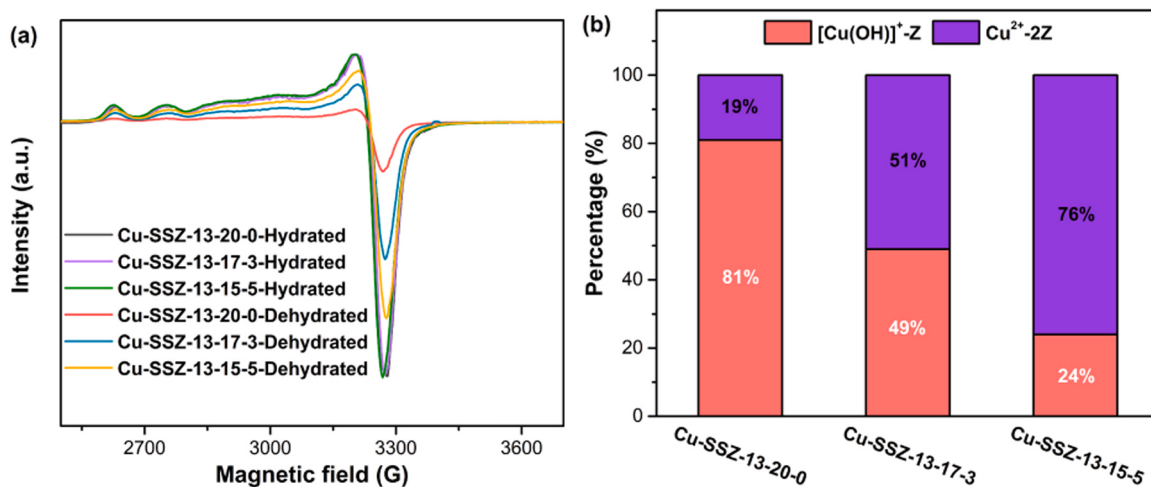


Fig. 11. (a) EPR spectra and (b) the quadratic integration results of Cu-SSZ-13-20-0, Cu-SSZ-13-17-3, and Cu-SSZ-13-15-5.

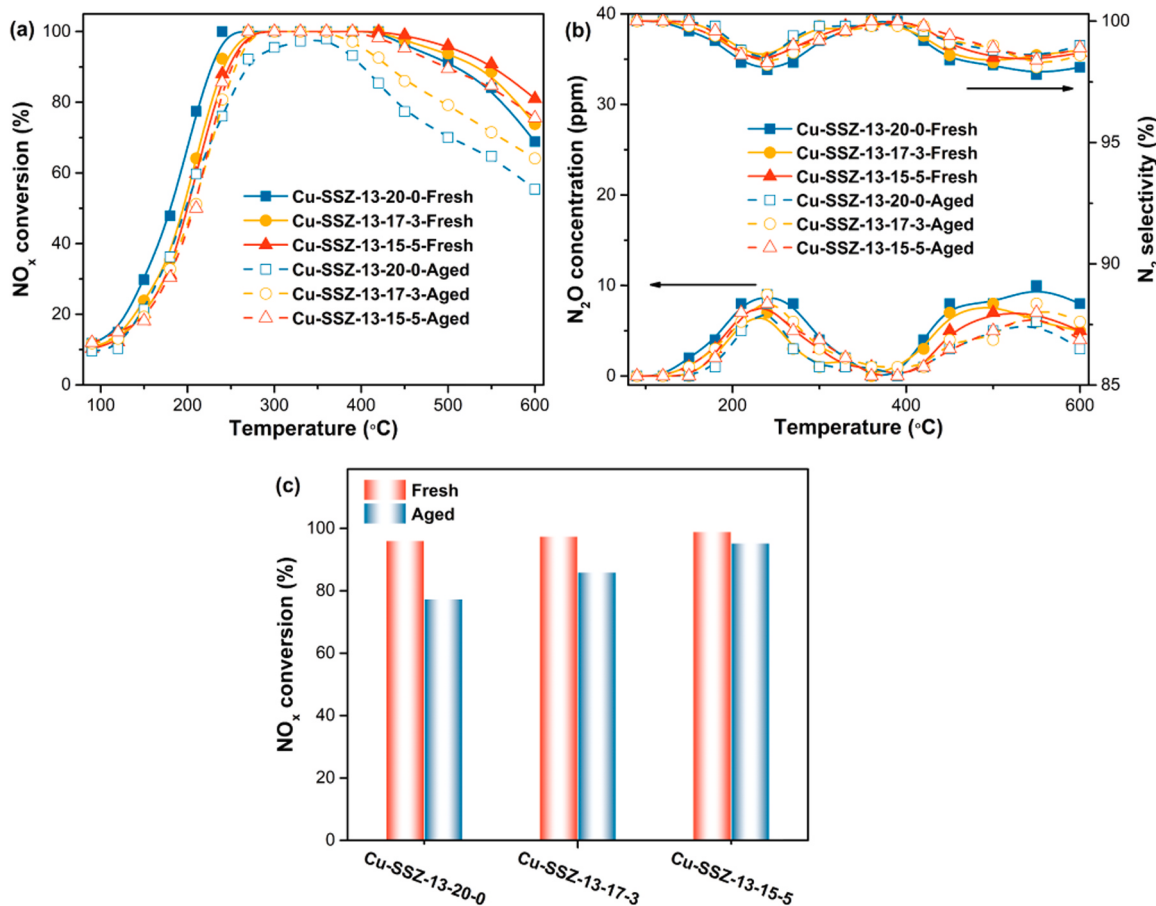


Fig. 12. (a)  $\text{NO}_x$  conversion and (b)  $\text{N}_2\text{O}$  concentration and  $\text{N}_2$  selectivity of different samples before and after hydrothermal aging; (c) SCR activity of all samples at 450  $^{\circ}\text{C}$  before and after hydrothermal aging. Reaction conditions: 500 ppm of NO, 500 ppm of  $\text{NH}_3$ , 3%  $\text{H}_2\text{O}$ , 5%  $\text{O}_2$ , balance  $\text{N}_2$  and GHSV = 150,000  $\text{h}^{-1}$ . Aged conditions: 800  $^{\circ}\text{C}$  with 10%  $\text{H}_2\text{O}/\text{N}_2$  for 12 h.

800  $^{\circ}\text{C}$  for 12 h. The  $\text{NO}_x$  conversion of Cu-SSZ-13-20-0 dropped obviously in the entire test range, specifically in the high temperature range (400–600  $^{\circ}\text{C}$ ), while the  $\text{NO}_x$  conversion of Cu-SSZ-13-15-5 only decreased slightly. All catalysts exhibit low  $\text{N}_2\text{O}$  yield and good  $\text{N}_2$  selectivity in the test range (Fig. 12b). Fig. 12c compares the  $\text{NO}_x$  conversion of the hierarchical Cu-SSZ-13 catalysts before and after hydrothermal aging at 450  $^{\circ}\text{C}$ . The decreasing tendency of  $\text{NO}_x$  conversion

rate after hydrothermal aging follows Cu-SSZ-13-20-0 (19.5%) > Cu-SSZ-13-17-3 (11.8%) > Cu-SSZ-13-15-5 (3.7%). This shows that compared with Cu-SSZ-13-20-0 synthesized using TMAda-OH as the template, the hydrothermal stability of hierarchical Cu-SSZ-13 synthesized using C<sub>16</sub>MPBr as a co-template is effectively improved. This increase in hydrothermal stability may be related to the following: (1) variety of catalyst wettability caused by the mesoporous system guided

by C<sub>16</sub>MPBr mesoporogen ; (2) difference of the destruction degree of zeolite framework under high-temperature hydrothermal ; (3) difference of the retention degree of the active copper species.

To compare the wettability of the hierarchical Cu-SSZ-13 catalysts, water vapor adsorption experiments were carried out. All samples are dehydrated before water vapor adsorption, and the relative humidity of the environment is guaranteed to be zero. The water vapor adsorption experiments were carried out under the condition of a relative humidity of 50%, and the results are shown in Fig. 13. The order of the weight gain rate of the three samples is as follows: Cu-SSZ-13-20-0 (14.5%) > Cu-SSZ-13-17-3 (13.3%) > Cu-SSZ-13-15-5 (12.7%). The lower weight gain rate indicates the better hydrophobicity of Cu-SSZ-13-15-5. This may be due to the enrichment of Si elements around the mesoporous channels and the scarcity of Al elements, thus constructing hydrophobic mesoporous channels. An attempt was made to prepare a sample with template ratio of TMAda-OH/C<sub>16</sub>MPBr = 10:10 (denoted as SSZ-13-10-10) to study the distribution of silicon and aluminum. The characterizations of SSZ-13-10-10 are shown in Fig. S7. It should be noted that SSZ-13-10-10 exhibits mesoporous characteristics but completely amorphous (do not show CHA structure) and the Si/Al ratio is 13. After being treated with 0.1 M HNO<sub>3</sub> solutions for 8 h at 80 °C, the obtained sample does not contain Al element. This indicates that the Al element hardly participates in the formation of the mesoporous region in this context. For comparison, using the same conditions to process H-SSZ-13-15-5, the Si/Al ratio (19.2) of the obtained sample is almost not change (not shown). This indicates that Al element will participate in the formation of CHA framework under the guidance of sufficient TMAda-OH, and the mesoporous region guided by C<sub>16</sub>MPBr is rich in Si element. This is consistent with the result that H-SSZ-13-15-5 contains almost no six-coordinated extra-framework Al observed by the <sup>27</sup>Al MAS NMR. This explains the good hydrophobicity of Cu-SSZ-13-15-5, and illustrates the more concentrated Al distribution of SSZ-13-17-3 and SSZ-13-15-5 after using C<sub>16</sub>MPBr as the mesoporogen.

The EPR experiments were performed on the samples after hydrothermal aging to monitor the existence and evolution of copper species, and the spectra are shown in Fig. 14a. Fig. S8 shows the comparison of EPR spectra of hydrated samples before and after hydrothermal aging. Compared with fresh samples, the relative signal intensity of the aged Cu-SSZ-13-20-0, Cu-SSZ-13-17-3 and Cu-SSZ-13-15-5 decreased by 33%, 17% and 7%, respectively. The decrease in signal intensity is ascribed to the EPR-silent CuO<sub>x</sub> species generated during the hydrothermal aging process. This further confirms by the DR UV-Vis spectra of the hierarchical Cu-SSZ-13 catalysts (Fig. S9), as the intensity of the absorption band (30,000–40,000 cm<sup>-1</sup>) attributed to the CuO<sub>x</sub> species in the spectrum of Cu-SSZ-13-20-0 after hydrothermal aging increases

significantly [48]. By quadratic integration of the EPR spectra of all catalysts, the relative proportions of the three types of copper species in all aging samples were obtained with the results are shown in Fig. 14b. For Cu-SSZ-13-20-0, a large amount of CuO<sub>x</sub> species (33%) is produced after hydrothermal aging, which implies that 33% of active copper species were lost, because many studies have shown that CuO<sub>x</sub> species display almost no contribution to the SCR reaction [49,50]. This is mainly because the high content of [Cu(OH)]<sup>+</sup>-Z species in the fresh Cu-SSZ-13-20-0 and they are more unstable than Cu<sup>2+</sup>-Z located in the 6MR sites, therefore, [Cu(OH)]<sup>+</sup>-Z species may easily reacts with water vapor. Previous studies have shown that this kind of unstable [Cu(OH)]<sup>+</sup>-Z species can be transformed into Cu<sup>2+</sup>-Z and CuO<sub>x</sub> species during the high-temperature hydrothermal treatment [15,33]. This can also explain the loss of numerous [Cu(OH)]<sup>+</sup>-Z species in the Cu-SSZ-13-20-0 sample and the increase of Cu<sup>2+</sup>-Z species after hydrothermal aging. For Cu-SSZ-13-15-5, due to the dominant distribution of copper species at 6MR sites caused by the high content of paired Al, the proportion of [Cu(OH)]<sup>+</sup>-Z species in the fresh sample is only 24%, thus, only about 7% of CuO<sub>x</sub> species were generated after hydrothermal aging. This indicates that about 93% of the active copper species in the Cu-SSZ-13-15-5 were reserved after hydrothermal aging. The difference in the content of active species could be an important reason why Cu-SSZ-13-15-5 maintains higher SCR activity after hydrothermal aging compared with Cu-SSZ-13-20-0.

To monitor the differences of the zeolite framework before and after hydrothermal aging, <sup>27</sup>Al and <sup>29</sup>Si MAS NMR experiments were performed on the aged hierarchical Cu-SSZ-13 catalysts. As shown in Fig. 15a, the intensity of features (58 ppm) attributed to the tetrahedral framework Al have different degrees of reduction for all aged samples. No signal attributable to six-coordinated extra-framework aluminum near 0 ppm was detected, which may be due to the interference of the paramagnetic copper species in the zeolites [15,51]. Taking the intensity of framework Al of fresh samples as a benchmark, the deconvolution of the spectra for all samples were normalized with the results are shown next to the spectra. It is found that the loss of framework Al for Cu-SSZ-13-20-0, Cu-SSZ-13-17-3 and Cu-SSZ-13-15-5 is 32.8%, 19.2% and 9.5%, respectively. This indicates that the zeolite framework of Cu-SSZ-13-20-0 was more severely damaged, which caused more degradation of framework Al. The <sup>29</sup>Si MAS NMR spectrum of aged Cu-SSZ-13-20-0 further confirms this, as the intensity of feature between – 102 and – 107 ppm declines obviously (Fig. 15b). This is mainly due to the following reasons. On one hand, compared with Cu-SSZ-13-15-5, Cu-SSZ-13-20-0 is more hydrophilic and therefore more likely to react with water. On the other, there are more unstable [Cu(OH)]<sup>+</sup>-Z species in Cu-SSZ-13-20-0 compared with Cu-SSZ-13-15-5. Therefore, more CuO<sub>x</sub> species were produced in Cu-SSZ-13-20-0 during the hydrothermal aging process. The CuO<sub>x</sub> species in the pores can combine with the framework Al to accelerate the degradation of the framework Al [52]. This is also confirmed by the study of Gao and co-workers [15,53], as they found that the degradation of the framework Al caused by the CuO<sub>x</sub> species is more serious than the direct reaction between water and the framework Al. Therefore, the more severely collapsed of the zeolite framework become another reason for the significant decrease in Cu-SSZ-13-20-0 SCR activity.

#### 4. Conclusion

In summary, hierarchical SSZ-13 catalysts were prepared through the collaborative effect of TMAda-OH and C<sub>16</sub>MPBr by a dual-template method. By cobalt ion titration method and the FTIR and DR UV-Vis spectra studies of cobalt-exchanged zeolites, we discovered that the introduction of C<sub>16</sub>MPBr into the crystalline gel can not only derive the mesoporous system, but also affect the framework Al arrangement of hierarchical SSZ-13. The distance between the framework Al sites in the hierarchical SSZ-13 shortens as the increases content of C<sub>16</sub>MPBr in the crystalline gel, that is, compared to SSZ-13-20-0, the density of paired Al

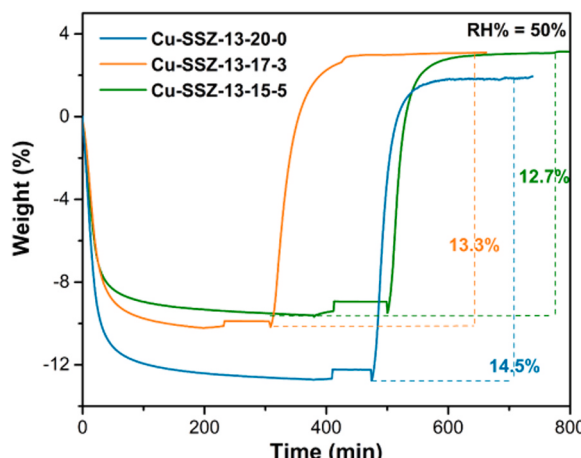


**Fig. 13.** Relative weight gain profiles of Cu-SSZ-13-20-0, Cu-SSZ-13-17-3, and Cu-SSZ-13-15-5.

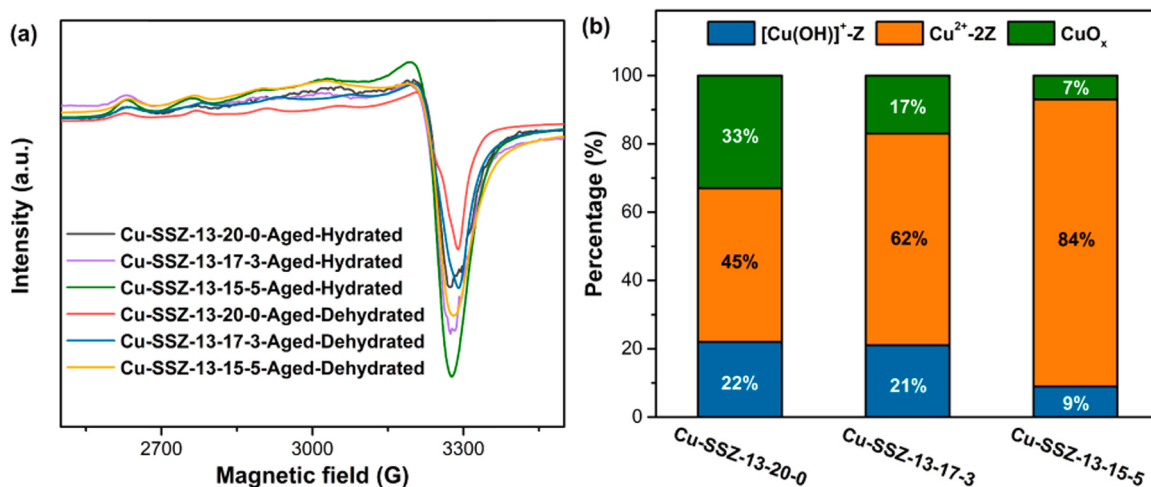


Fig. 14. (a) EPR spectra and (b) the quadratic integration results of Cu-SSZ-13-20-0, Cu-SSZ-13-17-3, and Cu-SSZ-13-15-5 after hydrothermal aging.

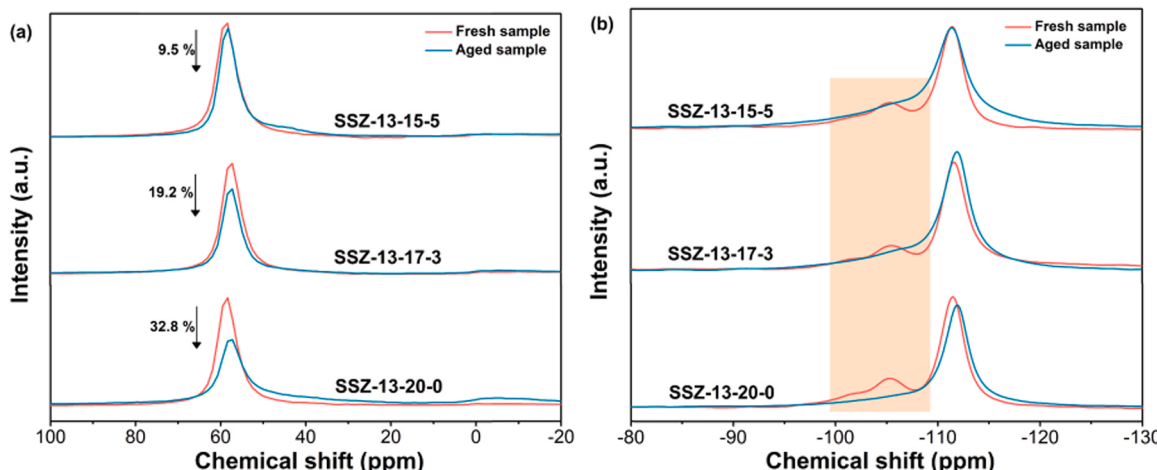


Fig. 15. (a)  $^{27}\text{Al}$  and (b)  $^{29}\text{Si}$  MAS NMR of hierarchical SSZ-13 before and after hydrothermal aging.

in the framework of SSZ-13-15-5 is significantly increased. This allows more active copper ions in Cu-SSZ-13-15-5 to occupy the cation sites of 6MR in the form of  $\text{Cu}^{2+} \text{-2Z}$  after copper ion-exchange. Because of the generation of numerous hydrothermally stable  $\text{Cu}^{2+} \text{-2Z}$  species, the loss of active copper species and dealumination of the framework in Cu-SSZ-13-15-5 can be avoided during severe hydrothermal aging. Therefore, compared to Cu-SSZ-13-20-0, the hydrothermal stability of Cu-SSZ-13-15-5 has been significantly improved. Our findings indicate that by adjusting the Al arrangement of the zeolite framework, the regulation of the distribution of copper active centers can be achieved, thereby affecting the catalytic performance for SCR of the catalyst.

#### CRediT authorship contribution statement

**Zhiqiang Chen:** Data curation, Investigation, Formal analysis, Writing – original draft, Writing – review & editing. **Tianle Ye:** Formal analysis. **Hongxia Qu:** Conceptualization, Supervision, Funding acquisition, Writing – review & editing. **Tenglong Zhu:** Validation, Methodology. **Qin Zhong:** Validation, Methodology.

#### Declaration of Competing Interest

The authors declare that they have no known competing financial interests or personal relationships that could have appeared to influence the work reported in this paper.

#### Acknowledgement

This work was financially supported by the National Natural Science Foundation of China (No. 51778296).

#### Conflicts of interest

There are no conflicts to declare.

#### Appendix A. Supporting information

Supplementary data associated with this article can be found in the online version at doi:10.1016/j.apcatb.2021.120867.

#### References

- [1] K. Khivantsev, N.R. Jaegers, L. Kovarik, J.C. Hanson, F. Tao, Y. Tang, X.Y. Zhang, I. Z. Koleva, H.A. Aleksandrov, G.N. Vayssilov, Y. Wang, F. Gao, J. Szanyi, Achieving atomic dispersion of highly loaded transition metals in small-pore zeolite SSZ-13: high-capacity and high-efficiency low-temperature CO and passive  $\text{NO}_x$  adsorbers, *Angew. Chem. Int. Ed.* 57 (2018) 16672–16677.
- [2] Y. Liu, W. Xue, S. Seo, X. Tan, D. Mei, C. Liu, I.-S. Nam, S. Hong, Water: a promoter of ammonia selective catalytic reduction over copper-exchanged LTA zeolites, *Appl. Catal. B Environ.* 294 (2021), 120244.
- [3] L. Han, S. Cai, M. Gao, J. Hasegawa, P. Wang, J. Zhang, L. Shi, D. Zhang, Selective catalytic reduction of  $\text{NO}_x$  with  $\text{NH}_3$  by using novel catalysts: state of the art and future prospects, *Chem. Rev.* 119 (2019) 10916–10976.

- [4] R. Li, Y. Zhu, Z. Zhang, C. Zhang, G. Fu, X. Yi, Q. Huang, F. Yang, W. Liang, A. Zheng, J. Jiang, Remarkable performance of selective catalytic reduction of NO<sub>x</sub> by ammonia over copper-exchanged SSZ-52 catalysts, *Appl. Catal. B Environ.* 283 (2021), 119641.
- [5] J. Tao, B. Li, Z. Lu, J. Liu, L. Su, Z. Tang, M. Li, Y. Xu, Endowing zeolite LTA superballs with the ability to manipulate light in multiple ways, *Angew. Chem. Int. Ed.* 59 (2020) 19684–19690.
- [6] B. Wang, Y. Mu, H. Zhang, H. Shi, G. Chen, Y. Yu, Z. Yang, J. Li, J. Yu, Red room-temperature phosphorescence of CDs@Zeolite composites triggered by heteroatoms in zeolite frameworks, *ACS Cent. Sci.* 5 (2019) 349–356.
- [7] X. Chi, M. Li, J. Di, B. Pu, L. Song, X. Wang, F. Li, S. Liang, J. Xu, J. Xu, A highly stable and flexible zeolite electrolyte solid-state Li-air battery, *Nature* 592 (2021) 551–557.
- [8] Y. Shan, J. Du, Y. Yu, W. Shan, X. Shi, H. He, Precise control of post-treatment significantly increases hydrothermal stability of in-situ synthesized cu-zeolites for NH<sub>3</sub>-SCR reaction, *Appl. Catal. B Environ.* 266 (2020), 118655.
- [9] E. Borfecchia, P. Beato, S. Svelle, U. Olsbye, C. Lamberti, S. Bordiga, Cu-CHA-a model system for applied selective redox catalysis, *Chem. Soc. Rev.* 47 (2018) 8097–8133.
- [10] Z. Chen, L. Guo, H. Qu, L. Liu, H. Xie, Q. Zhong, Controllable positions of Cu<sup>2+</sup> to enhance low-temperature SCR activity on novel Cu-Ce-La-SSZ-13 by a simple one-pot method, *Chem. Commun.* 56 (2020) 2360–2363.
- [11] S. Zhang, L. Pang, Z. Chen, S. Ming, Y. Dong, Q. Liu, P. Liu, W. Cai, T. Li, Cu/SSZ-13 and Cu/SAPO-34 catalysts for deNO<sub>x</sub> in diesel exhaust: current status, challenges, and future perspectives, *Appl. Catal. A Gen.* 607 (2020), 117855.
- [12] F. Gao, D. Mei, Y. Wang, J. Szanyi, C.H.F. Peden, Selective catalytic reduction over Cu/SSZ-13: linking homo- and heterogeneous catalysis, *J. Am. Chem. Soc.* 139 (2017) 4935–4942.
- [13] C. Paolucci, I. Khurana, A.A. Parekh, S. Li, A.J. Shih, H. Li, J.R.D. Iorio, J. D. Albaracin-Caballero, A. Yezers, J.T. Miller, W.N. Delgass, F.H. Ribeiro, W. F. Schneider, R. Gounder, Dynamic multinuclear sites formed by mobilized copper ions in NO<sub>x</sub> selective catalytic reduction, *Science* 357 (2017) 898–903.
- [14] J. Kwak, H. Zhu, J. Lee, C.H.F. Peden, J. Szanyi, Two different cationic positions in Cu-SSZ-13? *Chem. Commun.* 48 (2012) 4758–4760.
- [15] J. Song, Y. Wang, E. Walter, N. Washton, D. Mei, L. Kovarik, M. Engelhard, S. Prodinger, Y. Wang, C.H.F. Peden, F. Gao, Toward rational design of Cu/SSZ-13 selective catalytic reduction catalysts: implications from atomic-level understanding of hydrothermal stability, *ACS Catal.* 7 (2017) 8214–8227.
- [16] Y. Jangjou, Q. Do, Y. Gu, L.-G. Lim, H. Sun, D. Wang, A. Kumar, J. Li, L.C. Grabow, W.S. Epling, Nature of Cu active centers in Cu-SSZ-13 and their responses to SO<sub>2</sub> exposure, *ACS Catal.* 8 (2018) 1325–1337.
- [17] J. Du, Y. Shan, Y. Sun, M. Gao, Z. Liu, X. Shi, Y. Yu, H. He, Unexpected increase in low-temperature NH<sub>3</sub>-SCR catalytic activity over Cu-SSZ-39 after hydrothermal aging, *Appl. Catal. B Environ.* 294 (2021), 120237.
- [18] X. Ye, J.E. Schmidt, R.-P. Wang, I. Ravenhorst, R. Oord, T. Chen, F. Groot, F. Meirer, B. Weckhuysen, Deactivation of Cu-exchanged automotive-emission NH<sub>3</sub>-SCR catalysts elucidated with nanoscale resolution using scanning transmission X-ray microscopy, *Angew. Chem. Int. Ed.* 59 (2020) 15610–15617.
- [19] Y. Shan, J. Du, Y. Zhang, W. Shan, X. Shi, Y. Yu, R. Zhang, X. Meng, F.-S. Xiao, H. He, Selective catalytic reduction of NO<sub>x</sub> with NH<sub>3</sub>: opportunities and challenges of Cu-based small-pore zeolites, *Natl. Sci. Rev.* 8 (2021) nwab010.
- [20] F. Gao, E.D. Walter, E.M. Karp, J. Luo, R.G. Tonkyn, J. Kwak, J. Szanyi, C.H. F. Peden, Structure-activity relationships in NH<sub>3</sub>-SCR over Cu-SSZ-13 as probed by reaction kinetics and EPR studies, *J. Catal.* 300 (2013) 20–29.
- [21] F. Gao, N.M. Washton, Y. Wang, M. Kollar, J. Szanyi, C.H.F. Peden, Effects of Si/Al ratio on Cu/SSZ-13 NH<sub>3</sub>-SCR catalysts: implications for the active Cu species and the roles of Brønsted acidity, *J. Catal.* 331 (2015) 25–38.
- [22] J. Di Iorio, R. Gounder, Controlling the isolation and pairing of aluminum in chabazite zeolites using mixtures of organic and inorganic structure-directing agents, *Chem. Mater.* 28 (2016) 2236–2247.
- [23] J. Di Iorio, S. Li, C.B. Jones, C.T. Nimlos, Y. Wang, E. Kunkes, V. Vattipalli, S. Prasad, A. Moini, W.F. Schneider, R. Gounder, Cooperative and competitive occlusion of organic and inorganic structure directing agents within chabazite zeolites influences their aluminum arrangement, *J. Am. Chem. Soc.* 142 (2020) 4807–4819.
- [24] W. Lv, S. Wang, P. Wang, Y. Liu, Z. Huang, J. Li, M. Dong, J. Wang, W. Fan, Regulation of Al distributions and Cu<sup>2+</sup> locations in SSZ-13 zeolites for NH<sub>3</sub>-SCR of NO by different alkali metal cations, *J. Catal.* 393 (2021) 190–201.
- [25] J. Zhang, Y. Shan, L. Zhang, J. Du, H. He, S. Han, C. Lei, S. Wang, W. Fan, Z. Feng, X. Liu, X. Meng, F.-S. Xiao, Importance of controllable Al sites in CHA framework by crystallization pathways for NH<sub>3</sub>-SCR reaction, *Appl. Catal. B Environ.* 277 (2020), 119193.
- [26] X. Zhu, R. Rohling, G. Filonenko, B. Mezari, J.P. Hofmann, S. Asahina, E.J. M. Hensen, Synthesis of hierarchical zeolites using an inexpensive mono-quaternary ammonium surfactant as mesoporogen, *Chem. Commun.* 50 (2014) 14658–14661.
- [27] L. Liu, Z. Chen, H. Qu, J. Yuan, M. Yu, H. Xie, Q. Zhong, Dual-template assembled hierarchical Cu-SSZ-13: morphology evolution, crystal growth and stable high-temperature selective catalytic reduction performance, *CrystEngComm* 22 (2020) 7036–7045.
- [28] G. Kresse, J. Furthmuller, Efficient iterative schemes for Ab initio total-energy calculations using a plane-wave basis set, *Phys. Rev. B* 54 (1996) 11169–11186.
- [29] P. Honnenberg, W. Kohn, Inhomogeneous electron gas, *Phys. Rev. B* 136 (1964) B864–B871.
- [30] Z. Maeno, S. Yasumura, X. Wu, M. Huang, C. Liu, T. Toyao, K.I. Shimizu, Isolated indium-hydrides in CHA zeolites: speciation and catalysis for non-oxidative dehydrogenation of ethane, *J. Am. Chem. Soc.* 142 (2020) 4820–4832.
- [31] J. Wang, L. Shao, C. Wang, J. Wang, M. Shen, W. Li, Controllable preparation of various crystal size and nature of intra-crystalline diffusion in Cu/SSZ-13 NH<sub>3</sub>-SCR catalysts, *J. Catal.* 367 (2018) 221–228.
- [32] H. Zhao, Y. Zhao, Y. Ma, X. Yong, M. Wei, H. Chen, C. Zhang, Y. Li, Enhanced hydrothermal stability of a Cu-SSZ-13 catalyst for the selective reduction of NO<sub>x</sub> by NH<sub>3</sub> synthesized with SAPO-34 micro-crystallite as seed, *J. Catal.* 377 (2019) 218–223.
- [33] Z. Chen, L. Liu, H. Qu, B. Zhou, H. Xie, Q. Zhong, Migration of cations and shell functionalization for Cu-Ce-La/SSZ-13@ZSM-5: the contribution to activity and hydrothermal stability in the selective catalytic reduction reaction, *J. Catal.* 392 (2020) 217–230.
- [34] C. Fan, Z. Chen, L. Pang, S. Ming, X. Zhang, K.B. Albert, P. Liu, H. Chen, T. Li, The influence of Si/Al ratio on the catalytic property and hydrothermal stability of Cu-SSZ-13 catalysts for NH<sub>3</sub>-SCR, *Appl. Catal. A Gen.* 550 (2018) 256–265.
- [35] K. Mlekovaj, J. Dedecek, V. Pashkova, E. Tabor, P. Klein, M. Urbanova, R. Karcz, P. Szama, S.R. Whittleton, H.M. Thomas, A.V. Fishchuk, S. Sklenak, Al organization in the SSZ-13 zeolite. Al distribution and extraframework sites of divalent cations, *J. Phys. Chem. C* 123 (2019) 7968–7987.
- [36] L. Xie, F. Liu, X. Shi, F.-S. Xiao, H. He, Effects of post-treatment method and Na cocation on the hydrothermal stability of Cu-SSZ-13 catalyst for the selective catalytic reduction of NO<sub>x</sub> with NH<sub>3</sub>, *Appl. Catal. B Environ.* 179 (2015) 206–212.
- [37] R. Zhang, J.-S. McEwen, M. Kollar, F. Gao, Y. Wang, J. Szanyi, C.H.F. Peden, NO chemisorption on Cu/SSZ-13: a comparative study from infrared spectroscopy and DFT calculations, *ACS Catal.* 4 (2014) 4093–4105.
- [38] S.A. Bates, A.A. Verma, C. Paolucci, A.A. Parekh, T. Anggara, A. Yezers, W. F. Schneider, J.T. Miller, W.N. Delgass, F.H. Ribeiro, Identification of the active Cu site in standard selective catalytic reduction with ammonia on Cu-SSZ-13, *J. Catal.* 312 (2014) 87–97.
- [39] J. Dedecek, E. Tabor, S. Sklenak, Tuning the aluminum distribution in zeolites to increase their performance in acid-catalyzed reactions, *ChemSusChem* 12 (2019) 556–576.
- [40] P. Szama, E. Tabor, P. Klein, B. Wichterlova, S. Sklenak, L. Mokrzycki, V. Pashkova, M. Ogura, J. Dedecek, Al-rich Beta zeolites. distribution of Al atoms in the framework and related protonic and metal-ion species, *J. Catal.* 333 (2016) 102–114.
- [41] R. Karcz, J. Dedecek, B. Supronowicz, H.M. Thomas, P. Klein, E. Tabor, P. Szama, V. Pashkova, S. Sklenak, TNU-9 zeolite: aluminum distribution and extra-framework sites of divalent cations, *Chem. Eur. J.* 23 (2017) 8857–8870.
- [42] B.C. Knott, C.T. Nimlos, D.J. Robichaud, M.R. Nimlos, S. Kim, R. Gounder, Consideration of the aluminum distribution in zeolites in theoretical and experimental catalysis research, *ACS Catal.* 8 (2018) 770–784.
- [43] S. Li, H. Kong, W. Zhang, A density functional theory modeling on the framework stability of Al-rich Cu-SSZ-13 zeolite modified by metal ions, *Ind. Eng. Chem. Res.* 59 (2020) 5675–5685.
- [44] L. Xie, F. Liu, L. Ren, X. Shi, F.-S. Xiao, H. He, Excellent performance of one-pot synthesized Cu-SSZ-13 catalyst for the selective catalytic reduction of NO<sub>x</sub> with NH<sub>3</sub>, *Environ. Sci. Technol.* 48 (2014) 566–572.
- [45] H. Jiang, B. Guan, X. Peng, R. Zhan, H. Lin, Z. Huang, Influence of synthesis method on catalytic properties and hydrothermal stability of Cu/SSZ-13 for NH<sub>3</sub>-SCR reaction, *Chem. Eng. J.* 379 (2020), 122358.
- [46] E. Borfecchia, K. Lomachenko, F. Giordanino, H. Falsig, P. Beato, A. Soldatov, S. Bordiga, C. Lamberti, Revisiting the nature of Cu sites in the activated Cu-SSZ-13 catalyst for SCR reaction, *Chem. Sci.* 6 (2015) 548–563.
- [47] A. Godiksen, F.N. Stappen, P.N.R. Vennestrom, F. Giordanino, S.B. Rasmussen, L. F. Lundgaard, S. Mossin, Coordination environment of copper sites in Cu-CHA zeolite investigated by electron paramagnetic resonance, *J. Phys. Chem. C* 118 (2014) 23126–23138.
- [48] Z. Zhao, R. Yu, C. Shi, H. Gies, F.-S. Xiao, D.D. Vos, T. Yokoi, X. Bao, U. Kolb, R. McGuire, A.-N. Parvulescu, S. Maurer, U. Müller, W. Zhang, Rare-earth ion exchanged Cu-SSZ-13 zeolite from organotemplate-free synthesis with enhanced hydrothermal stability in NH<sub>3</sub>-SCR of NO<sub>x</sub>, *Catal. Sci. Technol.* 9 (2019) 241–251.
- [49] E. Borfecchia, K.A. Lomachenko, F. Giordanino, H. Falsig, P. Beato, A.V. Soldatov, S. Bordiga, C. Lamberti, Revisiting the nature of Cu sites in the activated CuSSZ-13 catalyst for SCR reaction, *Chem. Sci.* 6 (2015) 548–563.
- [50] H. Li, C. Paolucci, I. Khurana, L.N. Wilcox, F. Goltl, J.D. Albaracin-Caballero, A. J. Shih, F.H. Ribeiro, R. Gounder, W.F. Schneider, Consequences of exchange-site heterogeneity and dynamics on the UV-visible spectrum of Cu-exchanged SSZ-13, *Chem. Sci.* 10 (2019) 2373–2384.
- [51] S. Prodinger, M.A. Derewinski, Y. Wang, N.M. Washton, E.D. Walter, J. Szanyi, F. Gao, Y. Wang, C.H.F. Peden, Sub-micron Cu/SSZ-13: synthesis and application as selective catalytic reduction (SCR) catalysts, *Appl. Catal. B Environ.* 201 (2017) 461–469.
- [52] Y. Shan, W. Shan, X. Shi, J. Du, Y. Yu, H. He, A comparative study of the activity and hydrothermal stability of Al-rich CuSSZ-39 and Cu-SSZ-13, *Appl. Catal. B Environ.* 264 (2020), 118511.
- [53] A. Wang, Y. Chen, E.D. Walter, N.M. Washton, D. Mei, T. Varga, Y. Wang, J. Szanyi, Y. Wang, C.H.F. Peden, F. Gao, Unraveling the mysterious failure of Cu/SAPo-34 selective catalytic reduction catalysts, *Nat. Commun.* 10 (2019) 1137.